Detection and Characterization of Active Landslides with Multisource SAR Data and Remote Sensing in Western Guizhou, China

Yifei Zhu
  China University of Geosciences Beijing,shcool of

Xin YAO (✉ yaoxinphd@163.com)
  Chinese Academy of Geological Sciences State Key Laboratory of Continental Tectonics and Dynamics
  https://orcid.org/0000-0003-3063-2546

Leihua Yao
  China University of Geosciences Beijing School of Earth Sciences and Resources

Chuangchuang Yao
  Chinese Academy of Geological Sciences Institute of Exploration Techniques

Abstract

The western part of Guizhou is located in the second step of East Asia. Although the area is stratigraphically continuous and the surface is dominated by hard limestone and sandstone, catastrophic landslides often occur, seriously threatening residents' lives and the safety of property. Accurate identification of landslides and analysis of their developmental patterns are vital to prevent and reduce the threat of geological disasters. No active landslide survey data cover this region, so this paper identifies the active landslides in the western part of Guizhou by combining surface deformation information, multitemporal optical remote sensing images, geological lithology, and geomorphic features to obtain deformation information from multisource synthetic aperture radar surface data. This process increases the accuracy and reliability of identifying unstable slopes in areas with dense vegetation and steep terrain. By processing 283 Sentinel-1 and PALSAR-2 synthetic aperture radar data, 588 active landslides, 18 of which are high-risk large-scale landslides (landslide groups), are delineated for the first time in a range of 4.64×10^4 km^2 in the study area. The active landslides mainly include resurrected ancient landslides, reservoir/riverbank landslides, and mining-induced landslides, accounting for 2.4%, 4.1%, and 91.8%, respectively. The spatial distribution of landslides is banded along the cuesta at the edge of an outcrop of coal strata. Landslides are mainly distributed at elevations of 1800–2000 m, with an elevation difference of 50~100 m and a slope range of 35°~40°. The landslides are characterized by steep slopes, small scales, mass occurrences, and no dominant slope direction, classifying them as cuesta landslides induced by mining disturbance. Furthermore, nuanced remote sensing interpretation of the disaster elements, such as cuesta cliff, tensile cracks, deep and sizeable tensile channels, isolated rock masses, and collapse debris, and their processes of change, reveals that coal mining-disturbed landslides in this region have experienced four primary stages: natural unloading, mining disturbance, displacement acceleration, and slope failure. This is of great significance for understanding the genetic mechanism and developmental patterns, as well as the risk assessment, of this region.

1 Introduction

The Yunnan-Guizhou Plateau and its surrounding areas are the largest karst areas in the world (Huang and Cai 2007). In this area, Triassic hard sandstone and limestone overlie coal-bearing strata of the Permian Longtan Formation and Emeishan basalts, and their mechanical properties are prominently hard in the upper strata and soft in the lower strata. Because this area is located in the sloped transitional region between the first step of the Qinghai-Tibet Plateau and the third step of the hilly eastern plain, the interaction between tectonic activity and dissolution is strong, and cuesta landforms with steep upper and shallow lower slopes are widely distributed in this region (Li et al. 2020). The fragile geological environment and increasingly frequent human engineering activities have led to a wide distribution of geological disasters in this area, and heavy casualties occur periodically. For example, in 2010, the Gangwu landslide in Guanling County caused 99 deaths (Xing et al. 2015); in 2017, the Puasa landslide in Nayong County caused 26 deaths (Fan et al. 2019b); in 2019, the Jichang landslide in Shuicheng County caused 43 deaths (Zhao et al. 2020); and in 2004 and 2019, the Zuojiaying landslide in Nayong County caused a total of 47 deaths (Wang et al. 2020). These disasters are located in inaccessible high-altitude areas with steep

slopes, and early signs of disasters (range of deformation, surface cracks, etc.) are not easy to find; however, the process of slope failure is very intense and results in disaster bodies moving great distances, thereby posing a severe threat to the peripheral settlements. Therefore, it is vital to identify landslides accurately and analyze the pattern of development of landslides in this area to reduce and prevent the threat of geological disasters.

Existing research in the western Guizhou area has focused on disaster investigations only in areas with better observation conditions, or research has studied the failure mechanism (Carlà et al. 2018; Wang et al. 2021; Qu et al. 2021), movement process (Kang et al. 2017; Chen et al. 2020), and stability (Li 2019; Chen et al. 2021) of a single landslide. There is a lack of systematic surveys and investigations on the distribution characteristics, deformation patterns, and causes of landslide disasters in the western Guizhou region.

At present, optical remote sensing identification and synthetic aperture radar differential interferometry are reliable means for regional geological hazard investigation. Deformation markers, such as cracks, steep sides, uplifts, and subsidence, that are extracted from optical remote sensing can be used to quickly identify landslides that have experienced overall instability or have significant deformation markers (Xu et al. 2014; Li et al. 2019; Fan et al. 2019a). However, remote sensing image resolution limitations and cloud cover problems in Southwest China all bring challenges to optical remote sensing recognition. Synthetic aperture radar (SAR) differential interferometry can effectively detect the moving boundary and deformation rate of unstable geological bodies by calculating the phase differences of SAR images at different times in the same area and obtaining accurate deformation information within time intervals. Researchers have widely recognized the outstanding advantages of interferometric SAR (InSAR) in the field of landslide investigation and displacement monitoring. (Yao et al. 2017; Shi et al. 2020; Liu et al. 2021). However, in practice, the interference and incoherence caused by long temporal and spatial baselines, vegetation cover, and atmospheric delay all limit the use of differential InSAR (D-InSAR) technology.

This paper combines surface deformation information, multitemporal optical remote sensing imagery, lithology, and geomorphological features to map active landslides in western Guizhou, bridging the limitations of optical remote sensing and InSAR measurement techniques to identify landslides in areas with dense vegetation and steep terrain. The corresponding relationships between different types of active landslides and remote sensing spots are established, and their development and patterns of distribution are revealed. The use of multisource radar data overcomes the problem of missing recognition caused by shadowed areas in single orbit data. Multisource radar data increase the accuracy and reliability of the identification of unstable slopes. A comprehensive analysis of geological and geomorphic data and InSAR deformation results provides criteria for identifying landslide types. In addition, nuanced remote sensing interpretation of disaster elements, such as cuesta cliff, tensile cracks, deep and sizeable tensile channels, isolated rock masses, and collapse debris, and their processes of change, reveals that coal mining-disturbed landslides in this region have experienced four primary stages: natural unloading, mining disturbance, displacement acceleration and slope failure.

2 Study Area

The study area is located on the eastern side of the Yunnan-Guizhou Plateau in China and includes Lupanshui city and Bijie city in Guizhou Province (Fig. 1). The area's topography is high in the west and low in the east, with an elevation range of 1600–2700 m. The study area is characterized by significant river erosion and is a mid-mountain landscape. Geotectonically, it is part of the Yangtze Fold Belt. The study area has experienced complex tectonic activity and has been transformed by the Caledonian, Yanshan, and Xishan movements and the main existing tectonic traces are in the NW, NNE, and EW directions.

Proterozoic, Paleozoic, and Mesozoic strata are exposed in the study area (Fig. 2), in which limestone, sandstone, dolomite, and shale of Permian and Triassic shallow marine facies are the primary strata in this area.

The Permian strata are composed of medium-thick limestone, argillaceous siltstone, and coal. Among them, the Permian Longtan Formation (P_2l) is the primary coal-bearing strata in Southwest China; it contains 9–82 layers of coal that are interspersed between thin layers of chert limestone and argillaceous siltstone (Fig. 2). Coal mining activities are frequent in this area. In addition, under the influence of the Emeishan large igneous province, a set of thick-bedded massive basalts and basaltic volcanic breccia developed at the bottom of the Permian system in this area, and this set is mainly distributed in parts of Weining County in the western part of the study area and Panxian County in the southern part of the study area (Ali et al. 2005). The Triassic strata are composed of calcareous dolomite, medium-thick limestone, purplish-red sandstone and mudstone. Under different weathering conditions, the upper part of the strata forms a high steep slope or cliff, and the lower part forms a gentle slope; this pattern comprises the common upper steep and lower gentle landforms in Southwest China.

The study area has a subtropical monsoon climate with abundant water vapor, and rainfall is concentrated from May to September, which accounts for more than 80% of the annual rainfall. Affected by topography and circulation, precipitation decreases from southeast to northwest. The annual precipitation in the Liupanshui region in the southern part of the study area is 1300–1500 cm, while the Hezhang and Weining regions in the northern part of the study area are the low-rainfall areas in the province; these regions have annual rainfall totals of only 850–1050 cm, and the distribution of precipitation is extremely uneven.

3 Data And Methods

3.1 Data

Due to the severe shadows and layovers caused by topographic relief, SAR images in three observation directions are used to obtain ground deformation information to avoid landslide omission and misjudgment caused by spatiotemporal decorrelation to a great extent. The C-band Sentinel-1 ascending orbit images cover the period from January 9, 2019, to May 15, 2020, and consist of 4 screens with a total of 166 images. Sentinel-1 descending orbit data cover the period from January 11, 2019, to March 30, 2020, and consist of 2 screens with a total of 74 images. Sentinel-1 ascending and descending orbit data

cover the entire study area. The L-band PALSAR-2 image coverage period is from April 16, 2017, to August 19, 2018, and includes 6 screens with a total of 43 images. The blue rectangle marks the image coverage of PALSAR-2 radar in Fig. 1, and the SAR image parameter information used in the study area is shown in Table 1.

The one arc-second digital elevation model obtained by the Shuttle Radar Topography Mission (SRTM) is used for phase simulation, geocoding, shadow overlay analysis, and topographic factor (aspect, slope, elevation difference, and isoline data) generation of the whole terrain in the study area. The Google Earth platform provides optical remote sensing images at 0.3 m resolution for multiple periods between 2013 ~ 2015 for extracting surface landform features in the study area. Optical images (0.1 m resolution) acquired by unmanned aerial vehicle (UAV) aerial photography on December 20, 2019, were used for remote sensing identification of mining landslide deformation patterns. The lithologic, fault, and rock unit data are obtained from the 1:200000 geological map provided by the China Geological Survey.

Table 1
Radar image data parameters used in the study

SAR Sensor	Direction	Waveband	Spatial resolution	Angle of incidence	Heading angle	Image number	Temporal coverage
Sentinel-1	Ascending	C	2.32 × 13.98	39.6	-12.6	166	2019/01/04-2020/05/15
Sentinel-1	Descending	C	2.32 × 13.98	39.6	192.6	74	2019/01/11-2020/03/30
PALSAR-2	Ascending	L	1.43 × 2.12	36.1	-10.5	43	2017/04/16-2018/06/10

3.2 Methods

Catastrophic landslides often occur in cliff areas of cuestas disturbed by mining, which poses a severe threat to the villages and engineering facilities below. Therefore, accurate identification is needed. However, InSAR can identify only the mining deformation area but cannot accurately delineate the position, size, and outline of landslides in the subsidence area. Therefore, the InSAR annual deformation strength (Yao et al. 2020), annual deformation rate, optical remote sensing information, and geomorphological features are integrated to identify active landslides in this study.

First, multisource synthetic aperture radar images were collected and processed to obtain the annual deformation strength and velocity information in the study area. Second, optical remote sensing images were used to extract the position information of the landslide back wall, strewn steep ridge, and accumulation body. Finally, a deformation strength map of the study area, deformation positions extracted from optical remote sensing, and slopes in the study area were matched in the same coordinate system. Based on the annual average deformation strength, geomorphic features, and topographic data, the active landslides were identified, and the regional development patterns were analyzed.

3.1 Stacking-InSAR processing

Stacking-InSAR is a method for calculating the weighted average, unwrapping the differential interference phases and improving the deformation accuracy by minimizing atmospheric errors, noise phases and digital elevation model (DEM) errors (Strozzi et al. 2000). Unlike traditional D-InSAR, stacking-InSAR obtains the average shape variable within the stacking time baseline by phase stacking after obtaining multiple unwrapped differential interferograms. The basic assumption is that the atmospheric perturbation of each interference pattern is random, and the regional deformation is linear (Werner et al. 2003). This study aims to identify the potential range of activity in the study area but does not aim to obtain an accurate time series displacement curve of the point position. Therefore, in this study, the interferogram stacking method is used to obtain the annual deformation in the interference period.

The processing of stacking-InSAR proceeds as follows: first, images covering the study area are registered to the main image, and the interference combination is adjusted by setting time and space thresholds according to the band features of InSAR data to generate differential interferograms. PALSAR-2 images are in the L-band and are more favorable against the incoherence caused by large gradient deformation than the C-band Sentinel-1 image. To obtain high-quality differential interferograms, PALSAR-1 and Sentinel-1 image time baselines are set to 200 d and 60 d, respectively, with a spatial baseline value of 300 m for both. Second, the adaptive filtering algorithm is used to reduce the phase noise, and the terrain information and SAR data incidence angle are used to generate a shadow overlay to mask the interference data. The possible unwrapping errors are eliminated, and the minimum cost flow (MCF) algorithm is used to expand the phase value. Finally, the phase information within the stacking time baseline is obtained by stacking the phases of multiple differential interferences, and the phase information is converted into deformation quantity values to obtain the annual deformation rate in the study area.

4 Results And Analysis

4.1 Average deformation strength

Figure 3 shows the line-of-sight (LOS) annual deformation strength of the radar in the study area obtained from Sentinel-1 ascending orbit data. The distribution of deformation in the study area is extremely uneven. The deformation is concentrated in the central and southern parts, and several elliptical or banded deformation zones with lengths and widths greater than 1 km are developed. By comparing the three deformation strength results, the correlation coefficients of the ascending Sentinel-1 deformation rate, descending Sentinel-1 rate, and ascending PALSAR-2 rate are 0.417 and 0.375, respectively. The positive correlation of the three data indicates that the detection results have similar deformation patterns, and the overall movement direction is the same.

There are three main reasons for the low correlation. First, different observation angles lead to a significant difference in slope deformation values. Second, various bands have different InSAR measurement results for different deformation amplitudes; the L-band has a better measurement effect for large deformations, and the C-band may underestimate the deformation amount (Hu et al. 2014). Finally, there are differences in data coverage time. PALSAR-2 ascending orbit images cover the time from April 16, 2017, to June 10, 2018, and Sentinel-1 images cover January 2019 to May 2020 and January 2018 to March 2020. In

addition, coal mining activities in this region were interrupted for a short time in 2018, inevitably leading to differences in deformation values observed by different SAR data. Moreover, the primary purpose of this study is to effectively identify active landslides in the study area rather than monitor them. Therefore, the difference in deformation strength of the three datasets does not affect the interpretation results.

The Panxian area in the southern part of the research area has intense deformation (Fig. 4a, where a positive value indicates the direction of the surface close to the radar line-of-sight, and a negative value means that it is far away). The annual deformation rate illustrated by the cross-section of a typical banded deformation zone in this region shows that the maximum deformation is located in the center of the banded deformation zone and gradually decreases toward the edge, showing funnel-shaped settlement deformation (Fig. 4b and Fig. 4c) (Samsonov et al. 2013; Li et al. 2015). This deformation area is highly consistent with the distribution area of the primary coal strata in Southwest China—the Permian Longtan Formation (Fig. 2 and Fig. 3). Therefore, the banded or nearly elliptical deformation signals detected in the study area are identified as subsidence areas induced by underground coal mining.

4.2 Identification of active landslides

A total of 588 active landslides were identified within the study area of 4.64×10^4 km^2 by combining multisource SAR deformation maps, multitemporal optical remote sensing images, and slope information (Fig. 5); the spatial density was 0.0127 landslides/km^2. Among these landslides, 18 are high-risk landslides/landslide groups with large deformation rates (Table 2), which seriously threaten the residents below and require further investigation and monitoring. The unstable slopes identified in this study are consistent with those identified by other researchers in the study area (Wang et al. 2021). According to the distribution location, deformation characteristics, and lithology, active landslides can be classified into three types: resurrected ancient landslides, reservoir/riverbank landslides, and mining-induced landslides.

(1) **Resurrected ancient landslides.** This type of landslide is mainly distributed in the Weining-Liupanshui area in the northwestern part of the study area, and they have a slope range of 10°~20°. The primary lithology of the slip source is Permian Emeishan basalt. After intense weathering, the basalt surface layer in this region is characterized by surface loessification, shallow block cracking, and fissure opening due to weathering, which easily develop integral slip (Gao et al. 2020). The annual deformation rate of the annual deformation strength in 2019 ~ 2020 reveals an apparent armchair-shaped structure, and the overall deformation is mostly tongue-shaped. The long duration of deformation can be effectively recognized in multiphase interference images. Predisposing factors are rainfall or artificial activity. The deformation scale is large, the length is generally more than 800 m, and the width is more than 300 m. Figure 6 is the multisource recognition image of the Sanjiacun landslide, a typical resurrected ancient landslide in the study area, with coordinates of 103.82195° and 26.59618°. The Sanjiacun landslide is tongue-shaped on the plane, with two gullies developed on both sides and apparent armchair-shaped structural features at the back (Fig. 6c). Combined with the annual deformation maps (Figs. 6a, 6b), the landslide is identified as a resurrected ancient landslide. The Sentinel-1 ascending and descending orbit data show that there are apparent deformation traces in the middle and rear sources of the landslide. Field investigations reveal that there are tensile fractures in the back of the slope (Fig. 6d), and multiple tensile fractures (Fig. 6e, 6g) and

steep dips are developed in the middle of the slope (Fig. 6f). The locations of steep cracks correspond well with the results of InSAR deformation. A total of 14 resurrected ancient landslides are identified in the study area.

(2) **Reservoir or riverbank landslides.** This type of landslide is mainly distributed along the banks of the Sancha River and the Liuchong River in the middle of the study area. This type has a slope range of 10°~20° and relatively gentle terrain. The primary lithology of the slip source is the purplish-red mudstone developed in the Triassic system and the overlying Quaternary soil. Slope sliding as a whole occurs due to fluctuating river and reservoir levels. According to the annual deformation rate of 2019−2020, the deformation contours are mostly fan-shaped, and the deformation distribution is relatively concentrated. Large deformation gradients occur near the riverbank, and the multiphase image comparison shows that the deformation is greatly affected by the change in the water level. Figure 7 is the multisource recognition image of the Kuiqiao landslide, a typical reservoir landslide in the study area, with coordinates of 105.37868° and 26.541179°. In the middle of the landslide, vegetation is abundant, and the leading edge is the impounding area of the Pingzhai Reservoir. The optical image shows no apparent signs of deformation in this area (Fig. 7c). The landslide is located in the shadowed region of Sentinel-1 descending data, and no effective interference results are obtained. However, both the Sentinel-1 and ALOS PALSAR-2 ascending orbit data show significant landslide deformation. The annual deformation indicates that deformation of the overall slope is apparent, and the north side's deformation rate is more prominent (Fig. 7a, 7b). The field investigation reveals that a fault broke the road on the upper part of the north slope with a height of approximately 2 m (Fig. 7d). Several tensile fractures are developed along the road through the middle of the slope, with an extended length of 100−200 m (Fig. 7e, 7g). The front edge of the landslide is deformed at a considerable rate, and a deep and long extensional groove of approximately 1 m in width has developed on it, cutting through the main body of the landslide to form a dangerous landslide body (Fig. 7f). There is a good correspondence between the larger deformation location and the InSAR deformation pattern. In the study area, 24 reservoirs/riverbank landslides are identified.

(3) **Mining-induced landslides.** This type of landslide is mainly distributed in the Nayong-Shuicheng-Panxian area in the central and southern parts of the study area. Its spatial distribution is consistent with underground coal strata (Fig. 2 and Fig. 5), and this type is mainly caused by underground coal mining activities. The lithologies of the source are primarily sandy mudstone of the Triassic Feixianguan Formation and tuffs of the underlying Permian Longtan Formation. The sliding source is high and steep, with a slope range of 30°-70°. The annual deformation strength of this type is elliptical or banded and does not have an obvious landslide boundary. The deformation area usually spans the ridge or valley and is distributed along the mountain direction (Fig. 8a). The maximum deformation is concentrated in the middle of the area of deformation and is primarily located on high and steep faces of cuesta (Fig. 8b, 8c, and 8d). The deformation rate of this landslide type is higher than the two types mentioned above; the spatial distribution is dense and highly correlated with the distribution of mining subsidence areas. Landslide boundaries should be identified by optical remote sensing and field investigations.

Figure 8a shows the annual deformation strength of a typical mining-induced landslide. The annual deformation strength shows that the deformation area shows a striped pattern and is distributed along the

mountain direction. The deformation area spans mountain ridges and valleys, and there is no apparent landslide profile, so it is a typical mining deformation area. The deformation rate in the cliff area is relatively high, but the internal landslide morphology and boundary cannot be distinguished only by the annual deformation rate or annual deformation strength. Based on optical images and field investigation, 37 surface slides are developed in this area, 12 of which are deformed to varying degrees (Fig. 8b).

A total of 147 mining subsidence deformation areas are identified in the study area by optical remote sensing and annual deformation data, among which 37 mining-induced landslide groups are present, and 540 mining-induced landslides are developed, accounting for 91.8% of the total number of identified landslides.

Table 2
Statistics of 18 high-risk landslides in western Guizhou

No.	Landslide name	Longitude (°)	Latitude (°)	Length (m)	Width (m)	Maximum LOS rate (mm/a)	Landslide type
1	Tuojiyuanzi	104.6280	26.6633	750	710	45.000	Other
2	Xiamatian	103.8730	26.8815	918	770	39.000	Reactivated ancient landslide
3	Wujiapingzi	103.8290	26.8810	650	310	53.000	Reactivated ancient landslide
4	Sanjiacun	103.8210	26.5963	946	375	100.000	Reactivated ancient landslide
5	Laoyaying	104.0550	26.6948	1271	425	35.000	Reactivated ancient landslide
6	Kuaqiao	105.3860	26.5402	500	904	194.000	Reservoir landslide
7	Shiweicun	105.5590	27.0172	1728	1215	91.000	Reservoir landslide
8	Fumushan	104.9510	26.1865	635	195	65.000	Reservoir landslide
9	Duchuanzhai	104.9420	26.1758	1160	895	59.000	Reservoir landslide
10	Yangliucun	105.7650	27.5758	1881	816	118.000	Reservoir landslide
11	Yanjiaozhiai	105.5680	26.8608	480	575	79.000	Reservoir landslide
12	Zongling	105.2410	26.7141	7000	3000	208.000	Mining-induced landslide group
13	Yushe	104.7660	26.5022	2100	730	153.000	Mining-induced landslide group
14	Xinchang	104.5560	26.0529	4300	1700	286.000	Mining-induced landslide group
15	Songhe	104.6270	26.0383	5800	2500	188.000	Mining-induced landslide group
16	Luna	104.7870	25.9501	2000	850	126.000	Mining-induced landslide group
17	Baoshan	105.3050	26.7341	3890	1000	139.000	Mining-induced landslide group
18	Faer	104.8560	26.5316	1100	520	174.000	Mining-induced landslide group

4.3 Disaster distribution characteristics

The slope, aspect, elevation, and height difference of active landslide disasters in the study area are quantitatively analyzed by 30 m resolution DEM data (Fig. 9). The percentage of landslides number in each section and the percentage of natural area in each section are defined as LNP and NAP, respectively (Yao et al. 2020).

Landslide disasters in the study area are mainly developed at elevations of 1000 m-2200 m (Fig. 9a). In the range of 1000 m to 2000 m, the active landslide number increases with elevation. The percentage of active landslides decreases above an elevation of 2000 m. Therefore, the dominant elevation range in which landslides develop is established at an altitude of 1800 m-2000 m, and its LNP is 37.78%.

The relative height difference can reflect the relief degree of the study area and is the factor controlling the development of landslide disasters. With 500 m × 500 m as the calculation grid, the height difference between the highest point and the lowest point in each grid is taken as the overall height difference. The elevation difference is classified according to 50 m intervals, and the distribution map of the landslide elevation difference and the elevation difference of the whole area is obtained (Fig. 9b). When the elevation difference is greater than 50 m, the percentage of active landslides decreases with elevation. The proportion of landslides in the elevation difference range of 50–100 m is the highest, and the LNP and NAP are 34.36% and 30.39%, respectively.

The topographic slope is the dynamic condition that affects the occurrence of landslide disasters. A higher topographic slope provides favorable landslide transport conditions. Slopes in the study area are grouped (greater than 45° is one group, and the rest are grouped according to 5° spacing). The landslide percentage is evenly distributed in all sections between 5° and 25°, but the proportion is small (Fig. 9c). In the 25°-40° range, the LNP increases with increasing slope, reaching a peak in the 35°-40° range, and then decreases with increasing slope. In the 35°~40° region, LNP and NAP are 26.69% and 4.08%, respectively.

The slope direction can reflect the distribution of heat and rainfall in the region and then affect the distribution of landslides. The slope direction of the study area is zoned according to eight directions: N, NE, E, SE, S, SW, W, and NW. W-directed slopes account for a minor proportion, with LNP and NAP at 6.41% and 10.98%, respectively. Landslide hazards are relatively well developed in areas with slope directions of S and SE, and their LNPs are 15.77% and 15.42%, respectively (Fig. 9d).

The lithology and its characteristics form the material basis of landslide formation and occurrence. Different rock and soil bodies have different mechanical properties, and different lithologic combinations and slope structure types have different stabilities (Dai and Deng 2020). In the study area, landslides are mainly developed in the Triassic Feixianguan Formation (LNP of 28.07%) and Permian Dalong Formation (LNP of 24.21%), with small amounts distributed in the Carboniferous Datang Formation (LNP of 0.53%) and Maping Formation (LNP of 0.35%) (Fig. 9e).

According to the above statistics, the distribution of cuestas along edges of outcrops of coal strata, with elevations of 1800 ~ 2000 m, an elevation difference of 50 ~ 100 m, and slopes of 35°~40°, is the dominant geological and geomorphic combination for the development of active landslides. The landslides are characterized by a steep slope, small scale, mass occurrence, and no prevailing slope direction, reflecting the characteristics of cuesta landslides induced by mining disturbance.

4.4 Remote sensing recognition of the deformation mode of mining-induced landslides

Mining-induced landslides are the primary landslide type in the study area, accounting for 91.8%. Among them, the Zongling landslide group is characterized by a concentrated development and severe threat. Historically, many catastrophic landslides, with a total of 47 deaths, have occurred in the study area. Taking the Zongling landslide group as an example, the deformation mode of mining-induced landslides is identified by remote sensing.

The Zongling landslide group is located in Nayong County in the central part of the study area. It is a cuesta with a length of approximately 7 km, a height difference of 100 ~ 300 m, and a slope range of 60 ~ 80°. The strata lithologies from bottom to top are the Permian Longtan Formation (P_2l) and Changxing Formation (P_2c) coal, the Dalong Formation (P_2d) medium-thick limestone, the Triassic Feixianguan Formation (T_1f) dark purplish-pink siltstone, and tight limestone. Due to the mechanical properties of this lithologic combination, which are "soft at the bottom and hard at the top", cliffs formed in the upper part of the mountain under the effect of differential weathering, and a large number of cut and broken structural planes developed in the middle part of the mountain, while gentle slopes formed in the lower part. Such strata are widely distributed in Southwest China and are prone to landslides (Yin et al. 2011). Most importantly, the Longtan Formation stratum P_2l produces collapse zones due to repeated mining processes, inducing the formation of fracture zones and surface collapse in upper rock masses, which intensifies the deformation and damage of the slopes.

Due to the conditions of high susceptibility to ground disasters and long-term mining, active landslides are developed intensively in the Zongling area, which presents deformation and failure characteristics in various stages. Through high-resolution aeronautical data, details of disasters in the Zongling area were obtained (Fig. 10). Four stages of slope deformation were extracted and summarized: natural unloading (Fig. 11a), mining disturbance (Fig. 11b), displacement acceleration (Fig. 11c) and slope failure (Fig. 11d).

(1) **Natural unloading stage.** Under the influence of tectonic deformation, river erosion, and differential weathering, the upper part of the coal strata formed a cliff terrain with gentle and steep slopes (Fig. 10a, 10b). In the process of cliff formation, stress redistribution occurs on the surface of the slope body, surface rock body springback deformation occurs during unloading, a tensile stress area is formed at the top of the slope, and a plastic extrusion area is formed at the toe of the slope body; these characteristics form the internal factors of slope body deformation (Huang 2007). Some factors that accumulate in geological history are not conducive to slope stability (such as hard and soft lithologic combinations and gravity

stress) and cause the internal structural plane of the rock mass to develop considerably; as a result, the rock integrity declines, and the slope begins slowly deform.

(2) **Mining disturbance stage.** Underground coal mining causes argillaceous siltstone at the upper part of the goal roof to produce compressive stress concentrations, and the principal stresses on both sides of the coal wall are different. The adjustment and redistribution of such stress causes tension deformation of the overlying rock in the goaf (Zheng et al. 2015). The rock mass in the upper part of the roadway shears and slips along the structural plane and cracks, and vertical cracks develop in a small range in the upper rock mass of the roof. Under the influence of coal mining disturbance, the stress concentration at the top of the slope becomes more intense, and tensile cracks begin to appear on the surface to cut the slope rock mass (Fig. 10c, 10d).

(3) **Displacement acceleration stage.** With the continuous increase in the mining deformation area, large-scale caving occurs inside the goaf and forms a collapse zone (Chen et al. 2021). The upper rock mass of the roof is further compacted and gradually produces bending deformation, and the structural plane is further expanded. Vertical fractures develop in large numbers in the overburden and rapidly expand in the upper rock mass, and the internal structure of the slope appears loose. The tensile stress at the top of the slope is further concentrated, and the crack width at the top of the slope increases and continues to expand downward. At the top of the slope, cut and broken dangerous rock masses are gradually formed (Fig. 10e, 10f). With the increase in the horizontal displacement velocity of the fracture, the slope deforms as a whole, and the high and steep transit surface is accompanied by rockfall and minor collapse.

(4) **Slope failure stage.** Partial collapse occurs in the rock overlying the goaf, and there are still some deep and large grooves in the trailing edge (Fig. 10g, 10h). At this time, the crack at the top of the mountain expands inward and connects with the inner structural plane of the rock mass, and the dangerous rock mass enters the limit equilibrium state. The occurrence of a large amount of rainfall is a critical inducement of the overall slope instability (Zhu et al. 2019). Water enters the slope body along the surface cracks, softening the mudstone and sandstone and increasing the hydrostatic pressure inside the rock mass, leading to instability failure of the rock mass in the ultimate equilibrium state and forming collapse deposits in the gentle slope body at the bottom of the cliff (Fig. 10g, 10h).

5 Discussion

Due to the steep terrain in the study area, oblique beam irradiation of the surface causes shadows and layover to appear in the radar images, resulting in an invalid recognition area (Hu et al. 2014). In this study, multidirectional data were used to identify landslides; to some extent, this method compensated for the overlay and shadow problems caused by a single incident direction. However, omission and misjudgment caused by shadow and layover is still inevitable. The 30 m DEM data were used to carry out a quantitative calculation on the shadow area generated by the three data points used in this study. The shadow overlay area accounted for 0.9%. That is, there was still an area of approximately 419.4 km2 that could not be effectively identified.

Second, there are many cuestas and steep terrain in the study area. When two adjacent points in an SAR image are located at the top and bottom of a cliff, the interference phase produces a jump greater than π, resulting in an unwrapped error (Mondini et al. 2021). The phenomena of large gradient deformation and rapid deformation caused by mining can also produce interference and incoherence, resulting in mistranslation.

Finally, SAR adopts the side-view imaging mode, making the SAR system's sensitivity in the direction of satellite orbit very low. For landslides with slope directions similar to the azimuth, it is difficult to measure their movement along the slope direction using InSAR (Cascini et al. 2010). The data trajectory used in this study is nearly north-south because InSAR is less sensitive to landslide movement in the north-south direction. All of these factors can cause the omission of landslides.

6 Conclusion

In this paper, stacking-InSAR technology is used to identify active landslides in the western Guizhou area. On this basis, combined with the analysis of geomorphic features and geological conditions of a coal seam, the corresponding relationship between different types of active landslides and remote sensing images is established, their development and distribution patterns are revealed, and the following conclusions are drawn.

(1) Using InSAR technology and optical remote sensing images, 588 active landslides were identified in an area of 4.64×10^4 km^2 in western Guizhou. Active landslide disasters can be classified as resurrected ancient landslides, reservoir/riverbank landslides, and mining-induced landslides. Among them, 540 coal mining-induced landslides are identified, which are the main landslide types in this area.

(2) Landslides are mainly distributed at elevations of 1800 m-2000 m, with an elevation difference of 50 ~ 100 m and a slope range of 35°~40°. The landslides are characterized by steep slopes, small scales, mass occurrences, and no dominant slope direction, reflecting the characteristics of cuesta landslides induced by mining disturbance. Strengthening monitoring during the mining disturbance stage is the key to mining-induced landslide prevention and control.

(3) The combination of InSAR and optical remote sensing has great potential in the application of unstable slope boundaries and location identification in southwest mountainous areas. However, there is still an area of approximately 419.4 km^2 that cannot be effectively identified due to the shadow-overlying problem in mountainous regions. Multiband, multiangle and multiperiod high-resolution radar can effectively increase the comprehensiveness, dynamics, and accuracy of landslide identification and reduce landslide omission and misinterpretation.

(4) The disaster details of the Zongling landslide group were obtained through high-resolution UAV aerial photography data by extracting disaster elements, such as cuesta scarps, tension cracks, deep and large tension channels, isolated rock masses, and collapse debris, revealing that the coal mining-induced

landslides in the area experience four stages: natural unloading, mining disturbance, displacement acceleration, and slope failure.

7 Declarations

Acknowledgements

8 References

1. Ali JR, Thompson GM, Zhou M-F, Song X (2005) Emeishan large igneous province, SW China. Lithos 79:475–489. https://doi.org/10/b6jbwn

2. Carlà T, Farina P, Intrieri E, et al (2018) Integration of ground-based radar and satellite InSAR data for the analysis of an unexpected slope failure in an open-pit mine. Engineering Geology 235:39–52. https://doi.org/10/gc9fq4

3. Cascini L, Fornaro G, Peduto D (2010) Advanced low- and full-resolution DInSAR map generation for slow-moving landslide analysis at different scales. Engineering Geology 112:29-42. https://doi.org/10/dvw2bn

4. Chen L, Zhao C, Kang Y, et al (2020) Pre-Event Deformation and Failure Mechanism Analysis of the Pusa Landslide, China with Multi-Sensor SAR Imagery. Remote Sensing 12:856. https://doi.org/10/gjr374

5. Chen L, Zhao C, Li B, et al (2021) Deformation monitoring and failure mode research of mining-induced Jianshanying landslide in karst mountain area, China with ALOS/PALSAR-2 images. Landslides. https://doi.org/10/gj9m28

6. Dai F, Deng J (2020) Development characteristics of landslide hazards in Three-rivers basin of southeast Tibetan Plateau. Advanced Engineering Sciences 52(5):3–15. (in Chinese)

7. Fan X, Xu Q, Alonso-Rodriguez A, et al (2019a) Successive landsliding and damming of the Jinsha River in eastern Tibet, China: prime investigation, early warning, and emergency response. Landslides 16:1003–1020. https://doi.org/10/gg5cbf

8. Fan X, Xu Q, Scaringi G, et al (2019b) The "long" runout rock avalanche in Pusa, China, on August 28, 2017: a preliminary report. Landslides 16:139–154. https://doi.org/10/gg87xr

9. Gao Y, Li B, Gao H, et al (2020) Dynamic characteristics of high-elevation and long-runout landslides in the Emeishan basalt area: a case study of the Shuicheng "7.23"landslide in Guizhou, China. Landslides 17:1663–1677. https://doi.org/10/gg8zbb

10. Hu J, Li ZW, Ding XL, et al (2014) Resolving three-dimensional surface displacements from InSAR measurements: A review. Earth-Science Reviews 133:1–17. https://doi.org/10/f53bv3

11. Huang Q, Cai Y (2007) Spatial pattern of Karst rock desertification in the Middle of Guizhou Province, Southwestern China. Environ Geol 52:1325–1330. https://doi.org/10/ffsdzf

12. Huang RQ (2007) Large-scale landslides and their sliding mechanisms in china since the 20th century. Chinese Journal of Rock Mechanics and Engineering 26(3): 433–454. (in Chinese)

13. Kang Y, Zhao C, Zhang Q, et al (2017) Application of InSAR Techniques to an Analysis of the Guanling Landslide. Remote Sensing 9:1046. https://doi.org/10/gckw6m

14. Li B, Yin Y, Gao Y, et al (2020) Critical issues in rock avalanches in the karst mountain areas of southwest China. Hydrogeology & Engineering geology 47:5–13. (in Chinese)

15. Li L, Yao X, Yao J, et al (2019) Analysis of deformation characteristics for a reservoir landslide before and after impoundment by multiple D-InSAR observations at Jinshajiang River, China. Nat Hazards 98:719–733. https://doi.org/10/ghfgvk

16. Li W, Xu Q, Lu H, et al (2019) Tracking the deformation history of large-scale rocky landslide and its enlightenment. Geomatics and Information Science of Wuhan University 44:1043–1053. (in Chinese)

17. Li ZW, Yang ZF, Zhu JJ, et al (2015) Retrieving three-dimensional displacement fields of mining areas from a single InSAR pair. J Geod 89:17–32. https://doi.org/10/f6vp9b

18. Liu X, Zhao C, Zhang Q, et al (2021) Integration of Sentinel-1 and ALOS/PALSAR-2 SAR datasets for mapping active landslides along the Jinsha River corridor, China. Engineering Geology 284:106033. https://doi.org/10/gjr4sk

19. Mondini AC, Guzzetti F, Chang K-T, et al (2021) Landslide failures detection and mapping using Synthetic Aperture Radar: Past, present and future. Earth-Science Reviews 216:103574. https://doi.org/10/gj93fb

20. Qu F, Qiu H, Sun H, Tang M (2021) Post-failure landslide change detection and analysis using optical satellite Sentinel-2 images. Landslides 18:447–455. https://doi.org/10/gjr6zq

21. Samsonov S, d'Oreye N, Smets B (2013) Ground deformation associated with post-mining activity at the French–German border revealed by novel InSAR time series method. International Journal of Applied Earth Observation and Geoinformation 23:142–154. https://doi.org/10/gf4q86

22. Shi X, Zhang L, Zhong Y, et al (2020) Detection and Characterization of Active Slope Deformations with Sentinel-1 InSAR Analyses in the Southwest Area of Shanxi, China. Remote Sensing 12:392. https://doi.org/10/gg459x

23. Strozzi T, Wegmuller U, Werner C, Wiesmann A (2000) Measurement of slow uniform surface displacement with mm/year accuracy

24. Wang J, Wang C, Xie C, et al (2020) Monitoring of large-scale landslides in Zongling, Guizhou, China, with improved distributed scatterer interferometric SAR time series methods. Landslides 17:1777–1795. https://doi.org/10/gh2q6f

25. Wang Y, Liu D, Dong J, et al (2021) On the applicability of satellite SAR interferometry to landslide hazards detection in hilly areas: a case study of Shuicheng, Guizhou in Southwest China. Landslides. https://doi.org/10/gjr33f

26. Werner C, Wegmuller U, Strozzi T, Wiesmann A (2003) Interferometric point target analysis for deformation mapping

27. Xing A, Wang G, Li B, et al (2015) Long-runout mechanism and landsliding behaviour of large catastrophic landslide triggered by heavy rainfall in Guanling, Guizhou, China. Can Geotech J 52:971–981. https://doi.org/10/f7hzfh

28. Xu C, Xu X, Yao X, Dai F (2014) Three (nearly) complete inventories of landslides triggered by the May 12, 2008 Wenchuan Mw 7.9 earthquake of China and their spatial distribution statistical analysis. Landslides 11:441–461. https://doi.org/10/f55sfk

29. Yao X, Deng J, Liu X, et al (2020) Primary recognition of active landslides and development rule analysis for pan Three-river-parallel Territory of Tibet Plateau. Advanced Engineering Sciences 52(5):16–37. (in Chinese)

30. Yao X, Li L, Zhang Y, et al (2017) Types and characteristics of slow-moving slope geo-hazards recognized by TS-InSAR along Xianshuihe active fault in the eastern Tibet Plateau. Nat Hazards 88:1727–1740. https://doi.org/10/gbtsmb

31. Yin Y, Sun P, Zhang M, Li B (2011) Mechanism on apparent dip sliding of oblique inclined bedding rockslide at Jiweishan, Chongqing, China. Landslides 8:49–65. https://doi.org/10/cf3dnx

32. Zhao W, Wang R, Liu X, et al (2020) Field survey of a catastrophic high-speed long-runout landslide in Jichang Town, Shuicheng County, Guizhou, China, on July 23, 2019. Landslides 17:1415–1427. https://doi.org/10/gg8zbj

33. Zheng D, Frost JD, Huang RQ, Liu FZ (2015) Failure process and modes of rockfall induced by underground mining: A case study of Kaiyang Phosphorite Mine rockfalls. Engineering Geology 197:145–157. https://doi.org/10/f7wx6m

34. Zhu Y, Xu S, Zhuang Y, et al (2019) Characteristics and runout behaviour of the disastrous 28 August 2017 rock avalanche in Nayong, Guizhou, China. Engineering Geology 259:105154. https://doi.org/10/gjr6zt
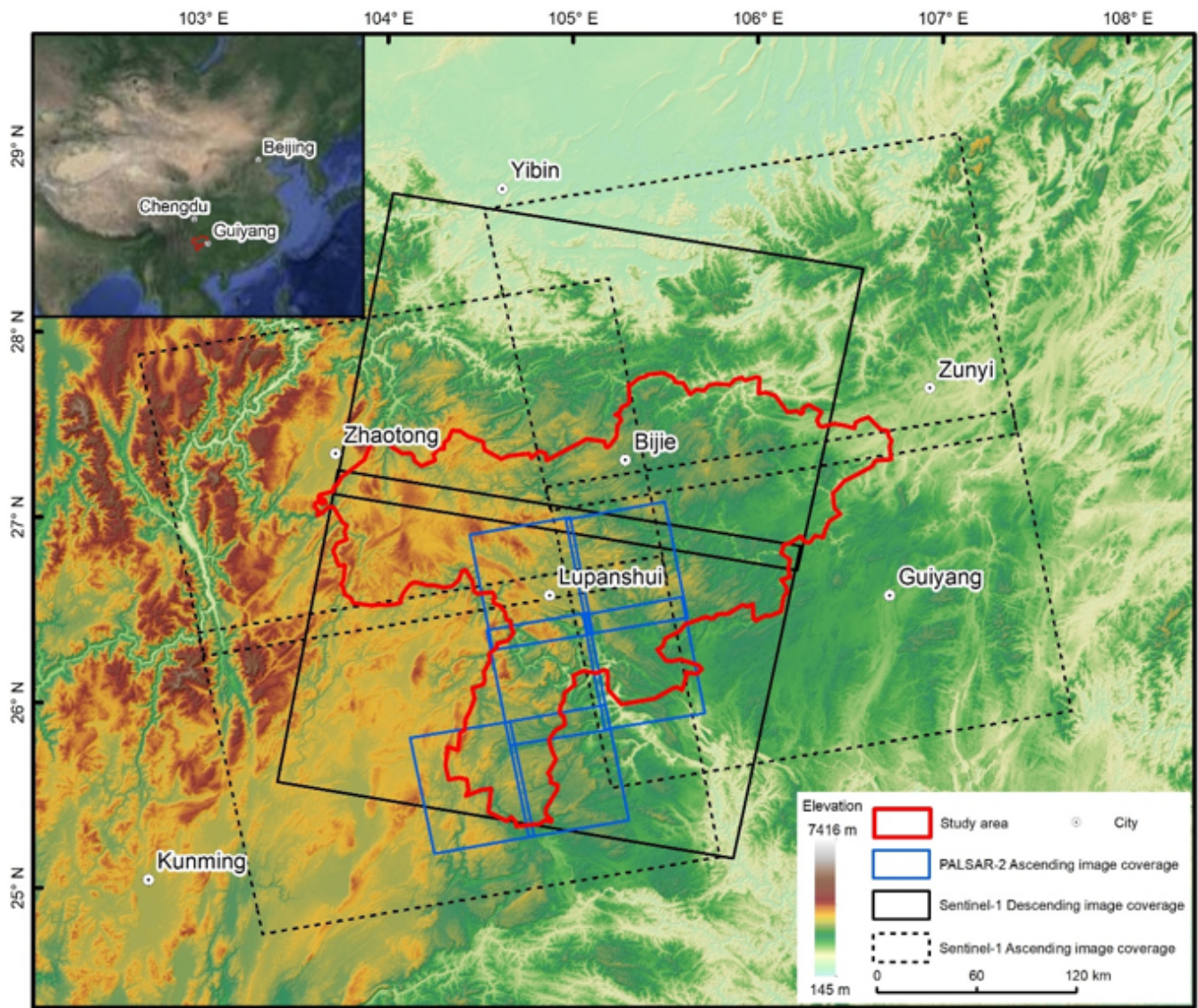
Figures

Figure 1

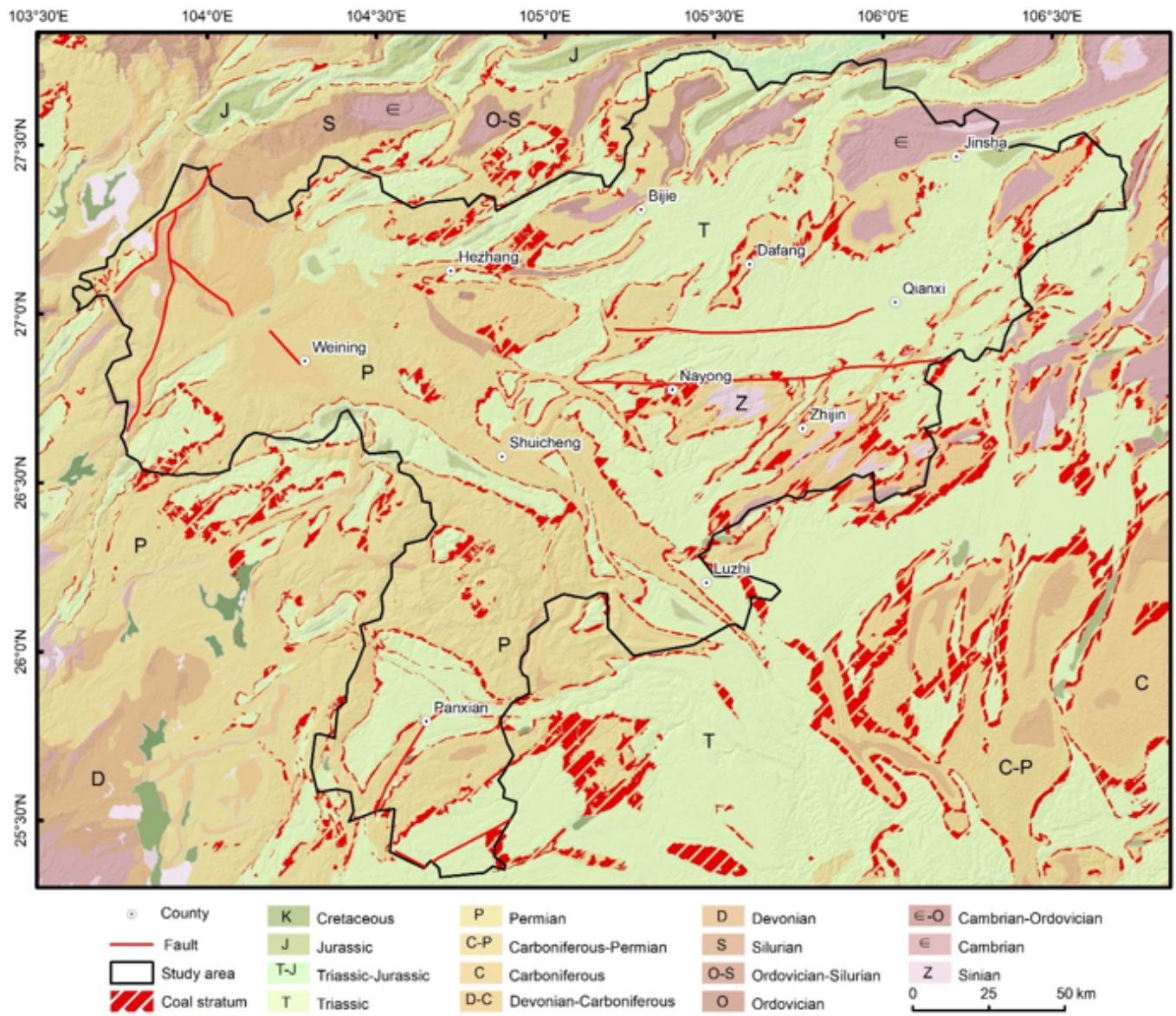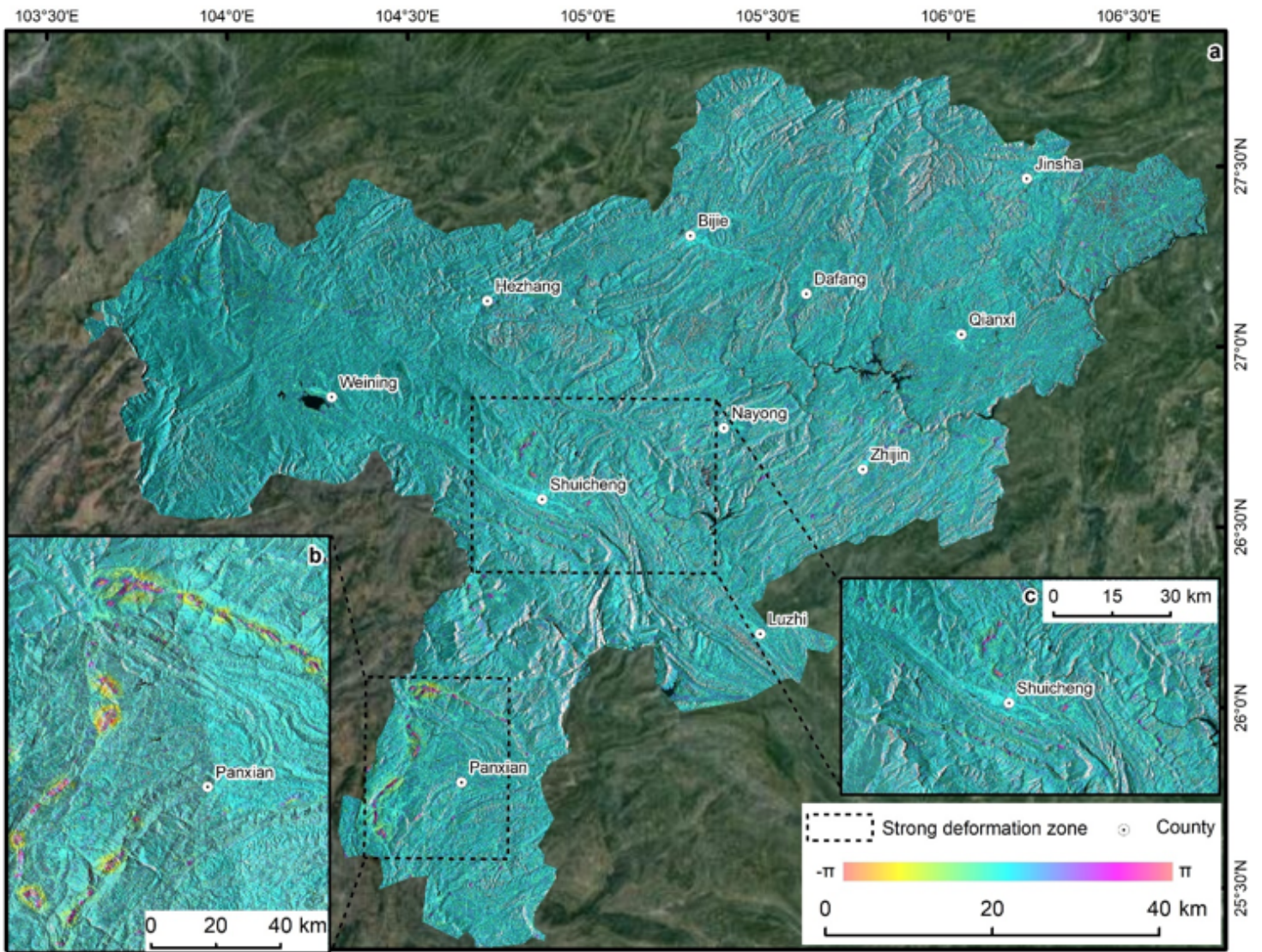Location of the study area and data coverage

Figure 2

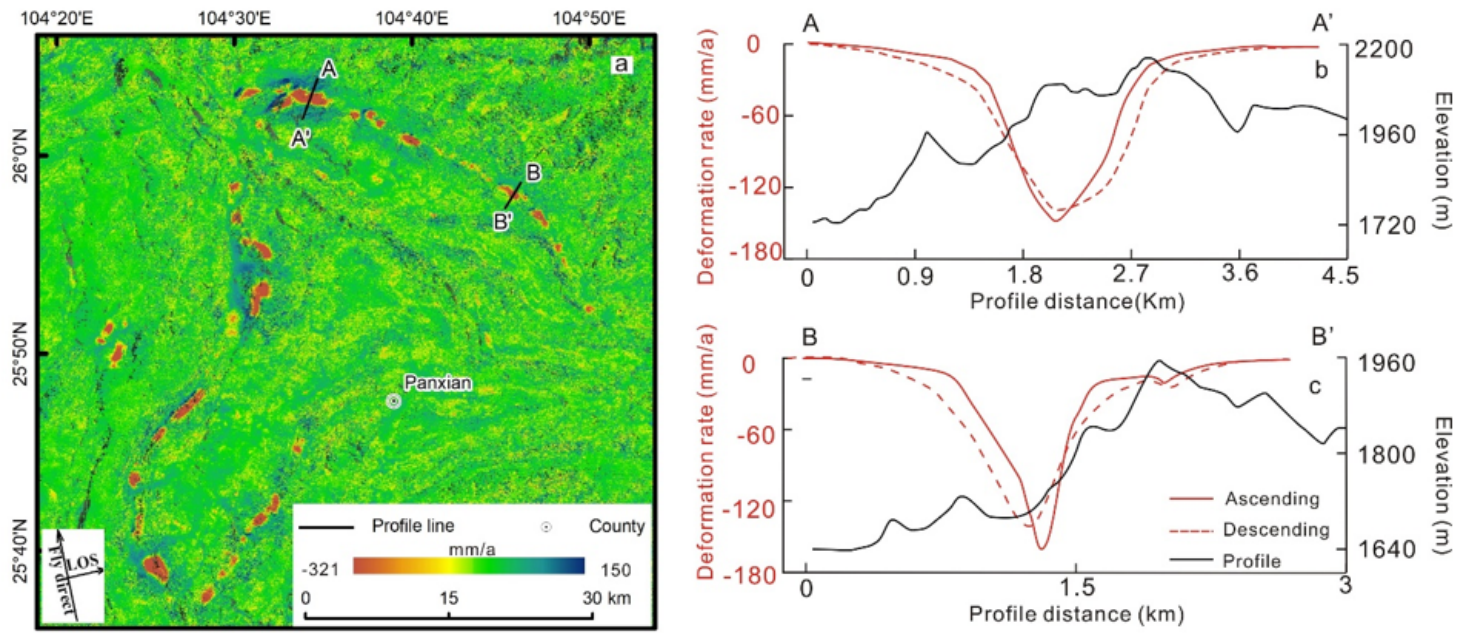Geological map of the study area

Figure 3

Annual deformation strength from 2019-2020; (a) in study area; (b) in the Pan County area; (c) in the Shuicheng County area

Figure 4

a; Annual deformation rate in 2019-2020 in Panxian; (b, c) profiles showing the deformation rate of typical mining subsidence in Panxin Note: To better display the deformation results, the display range of the color bar in panel A is -321~150 mm/a, but the deformation still reaches 510 mm/a in some locations.
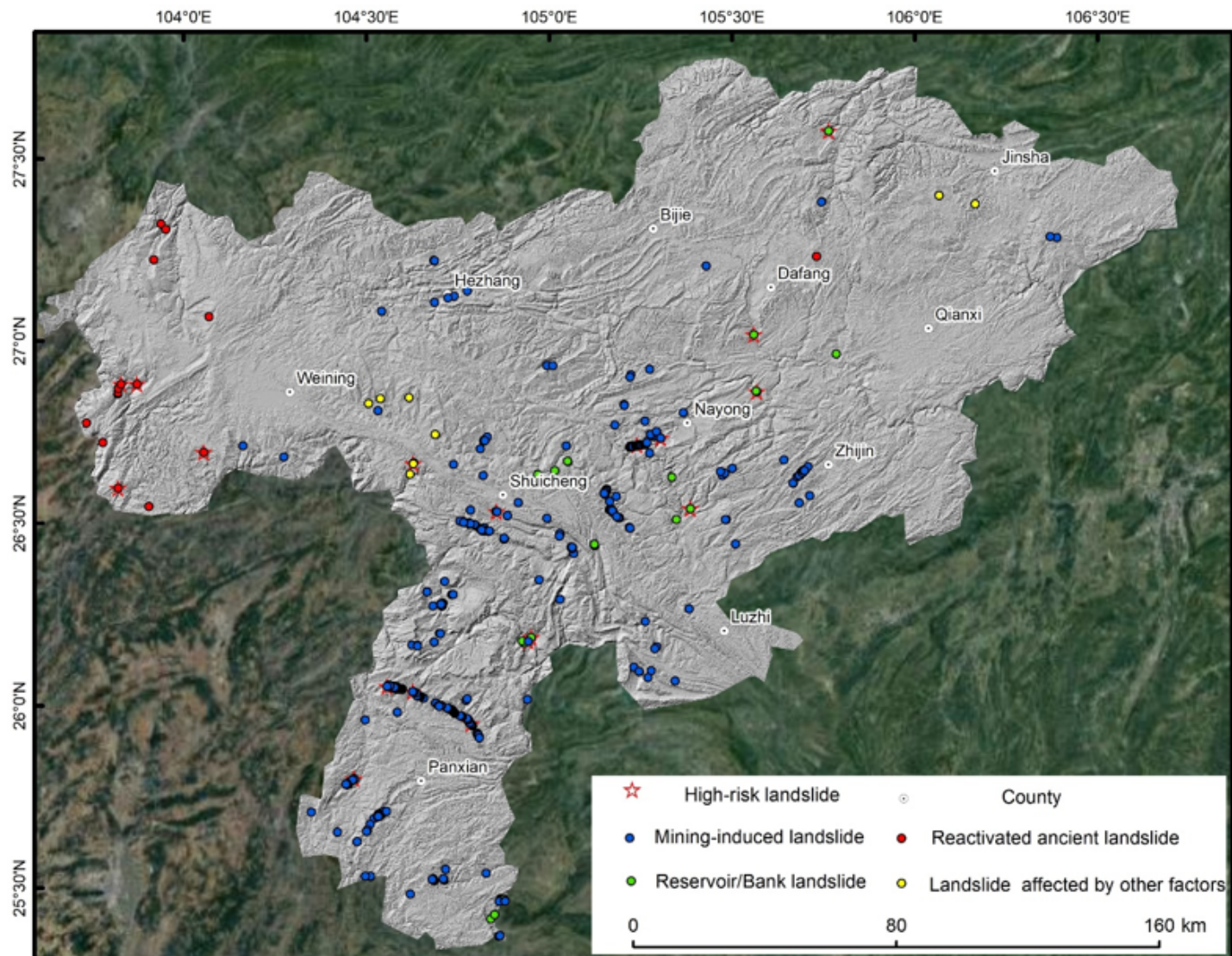
Figure 5

Active landslides distribution map
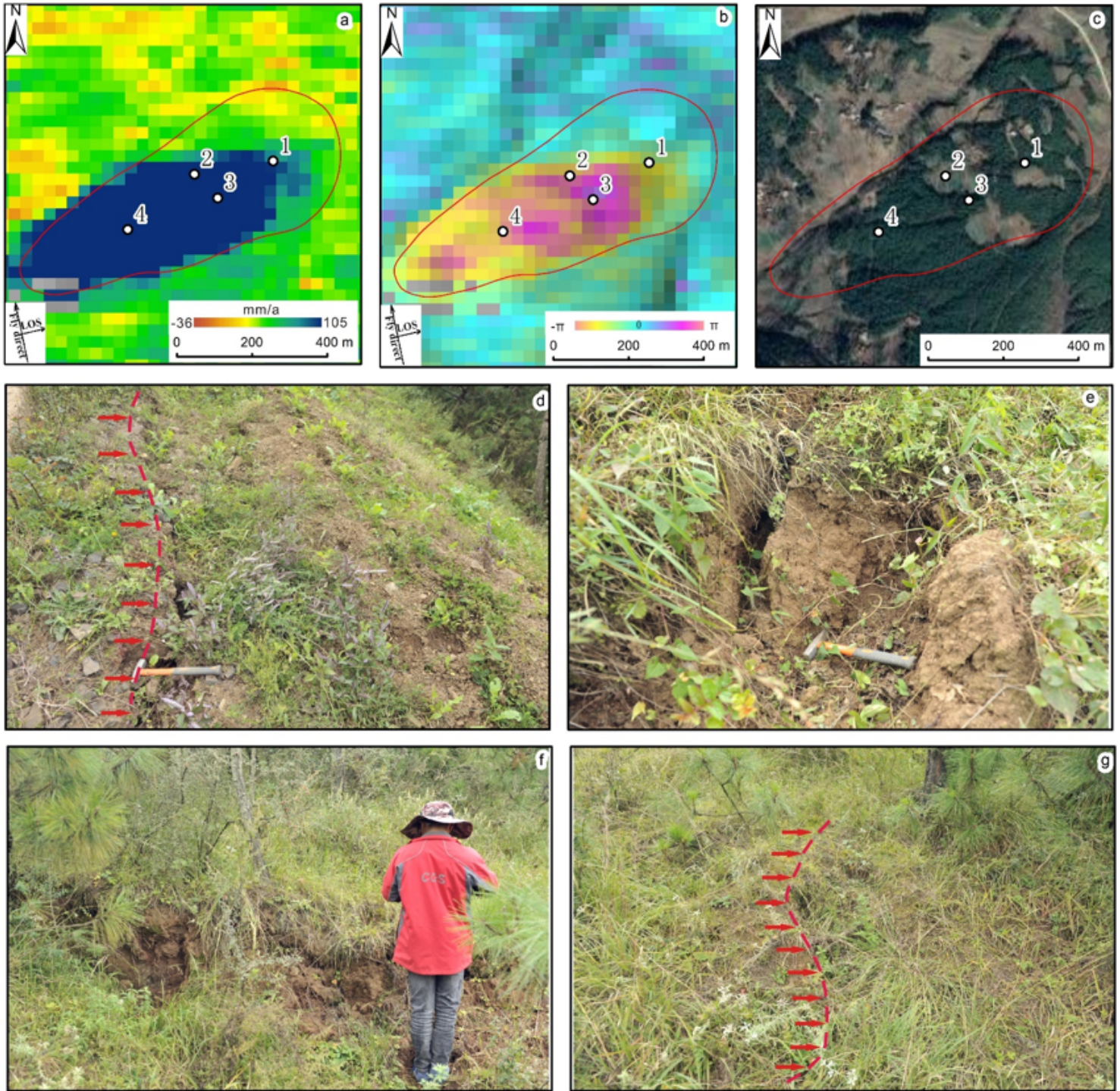
Figure 6

Multisource recognition image of the resurrected ancient landslide (taking Sanjia village as an example); (a) annual deformation rate derived from the Sentinel-1 ascending orbit; (b) annual deformation strength derived from the Sentinel-1 ascending orbit; (c) panorama; (d~g) field photos of points 1 to 4
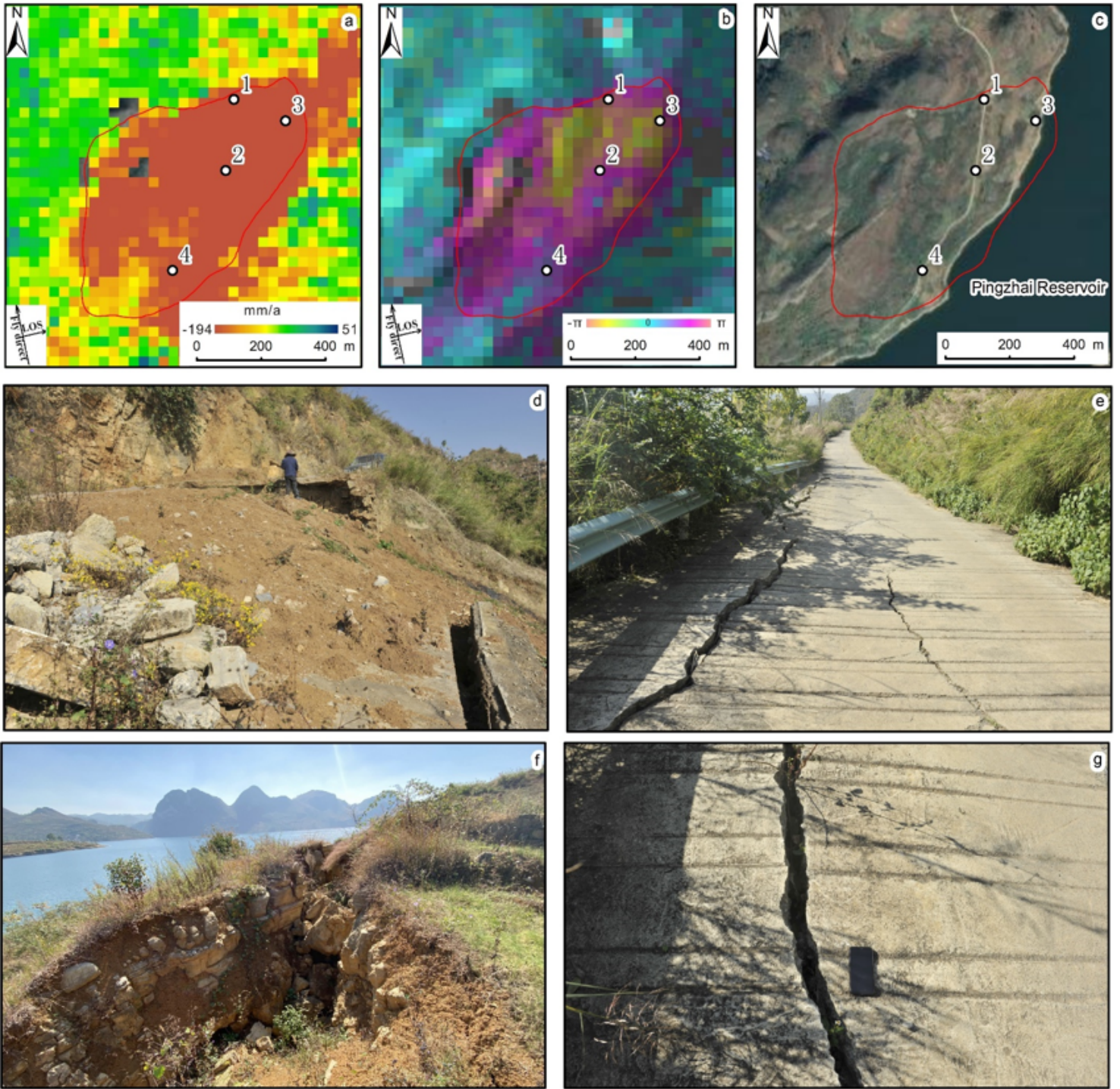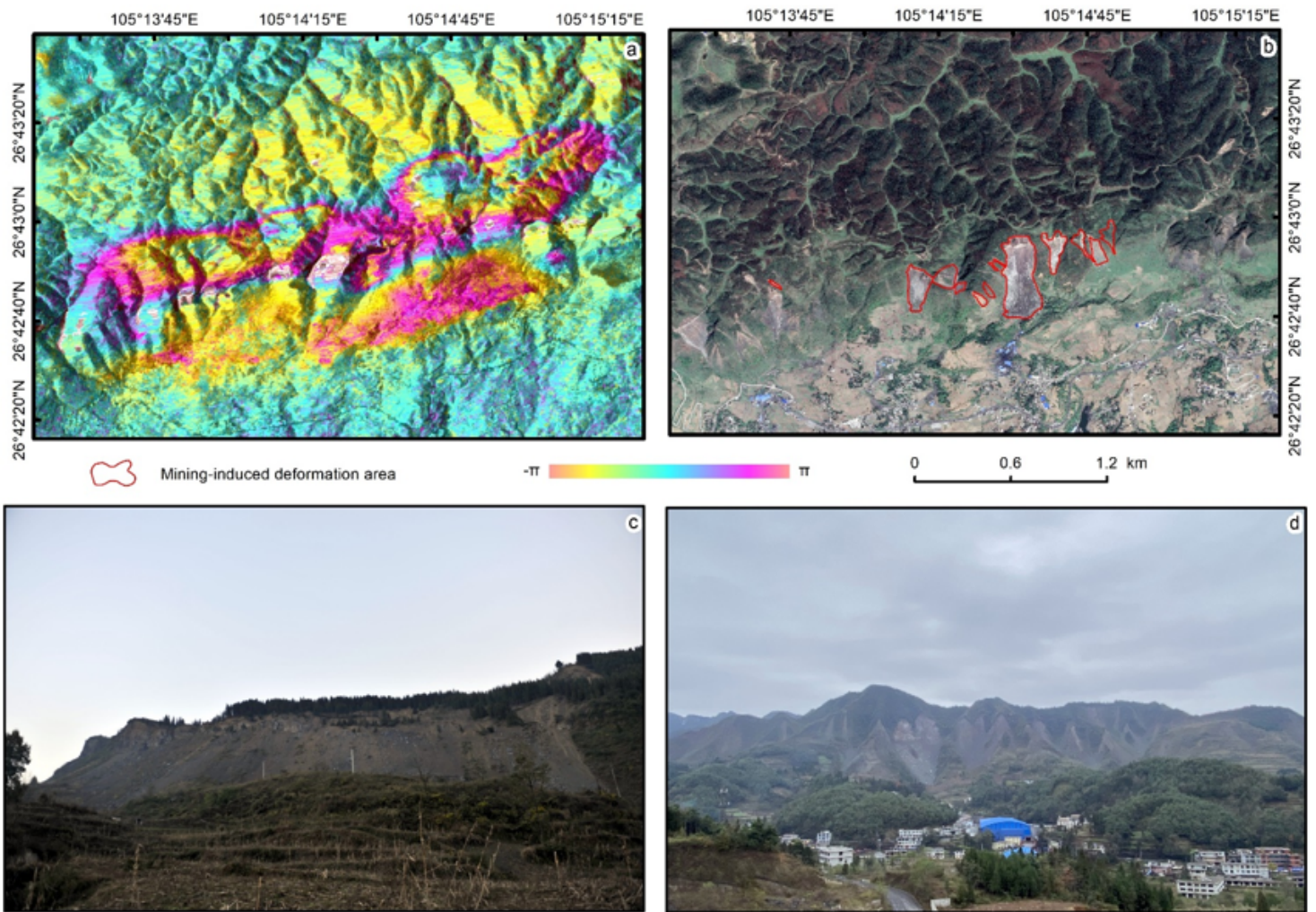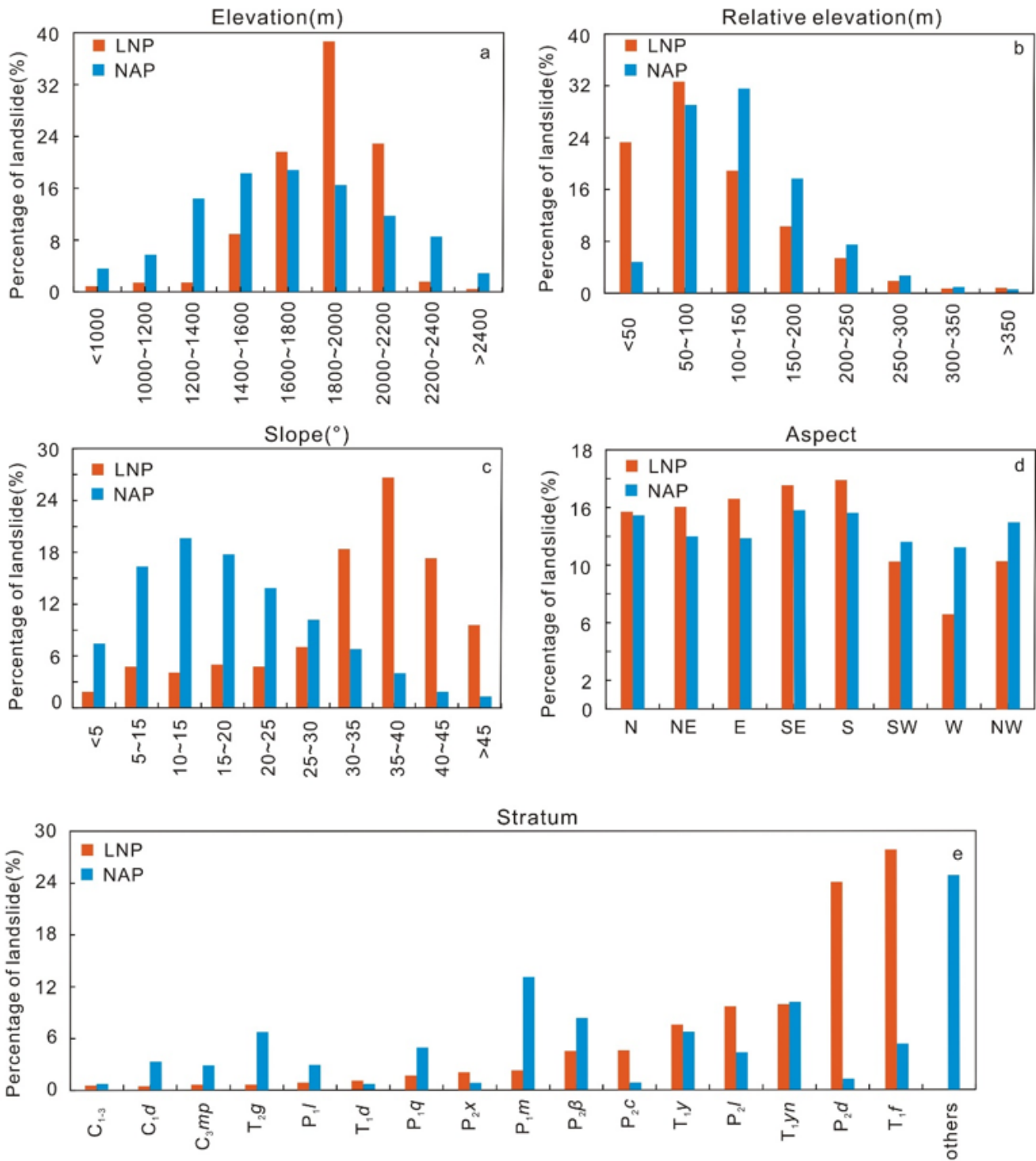
Figure 7

Multisource recognition image of reservoir or riverbank landslides (taking Kuiqiao as an example); (a) annual deformation rate derived from the Sentinel-1 ascending orbit; (b) annual deformation strength derived from the Sentinel-1 ascending orbit; (c) panorama; (d~g) field photos of points 1 to 4
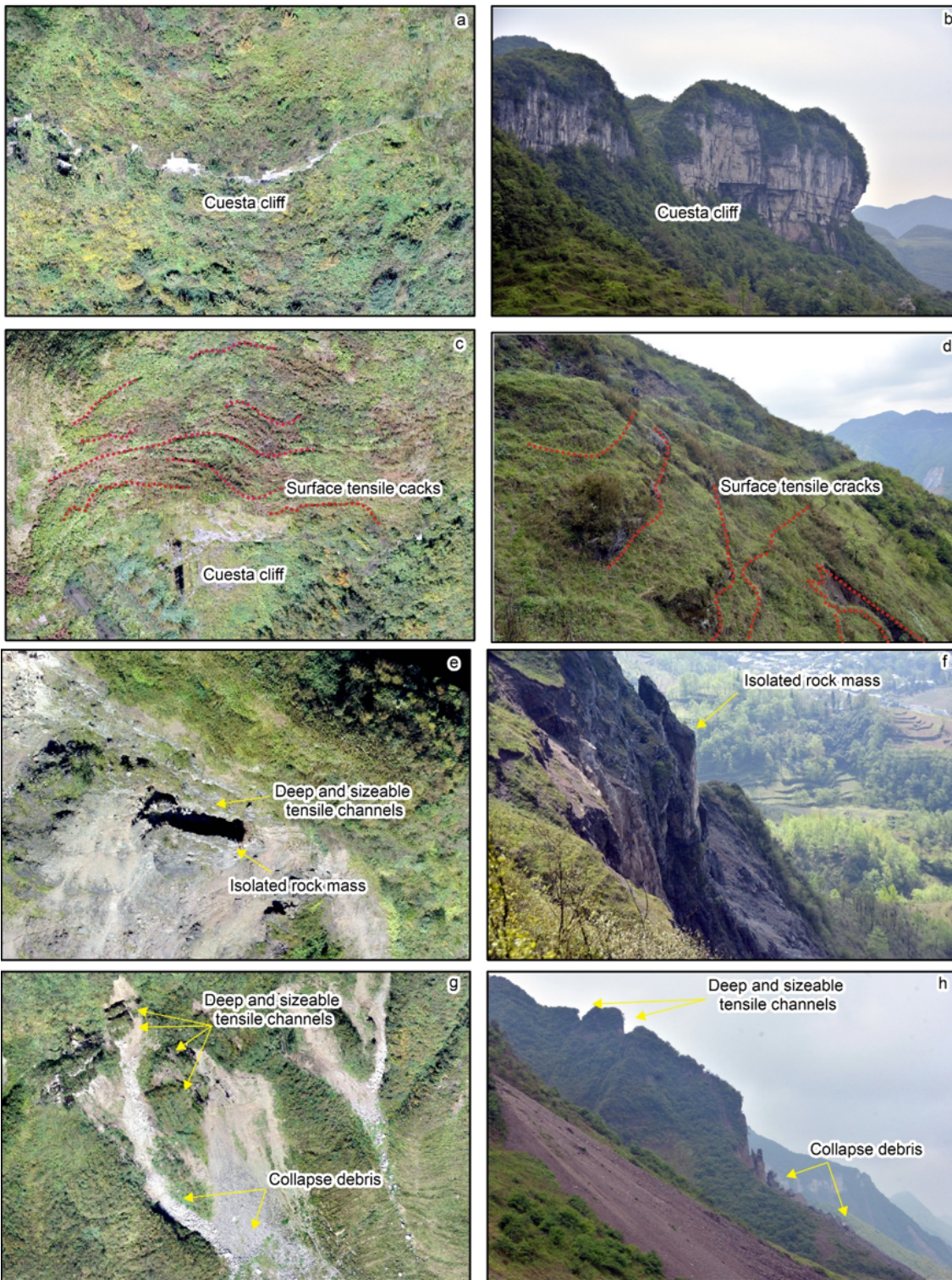
Figure 8

Annual deformation strength of a typical mining-induced landslide; (b, c, and d) field survey photos of typical landslide groups in the study area

Figure 9

Statistics of geomorphological elements of active landslides in the study area; distribution ratio of (a) elevation; (b) relative elevation; (c) slope; (d) aspect; (e) stratum
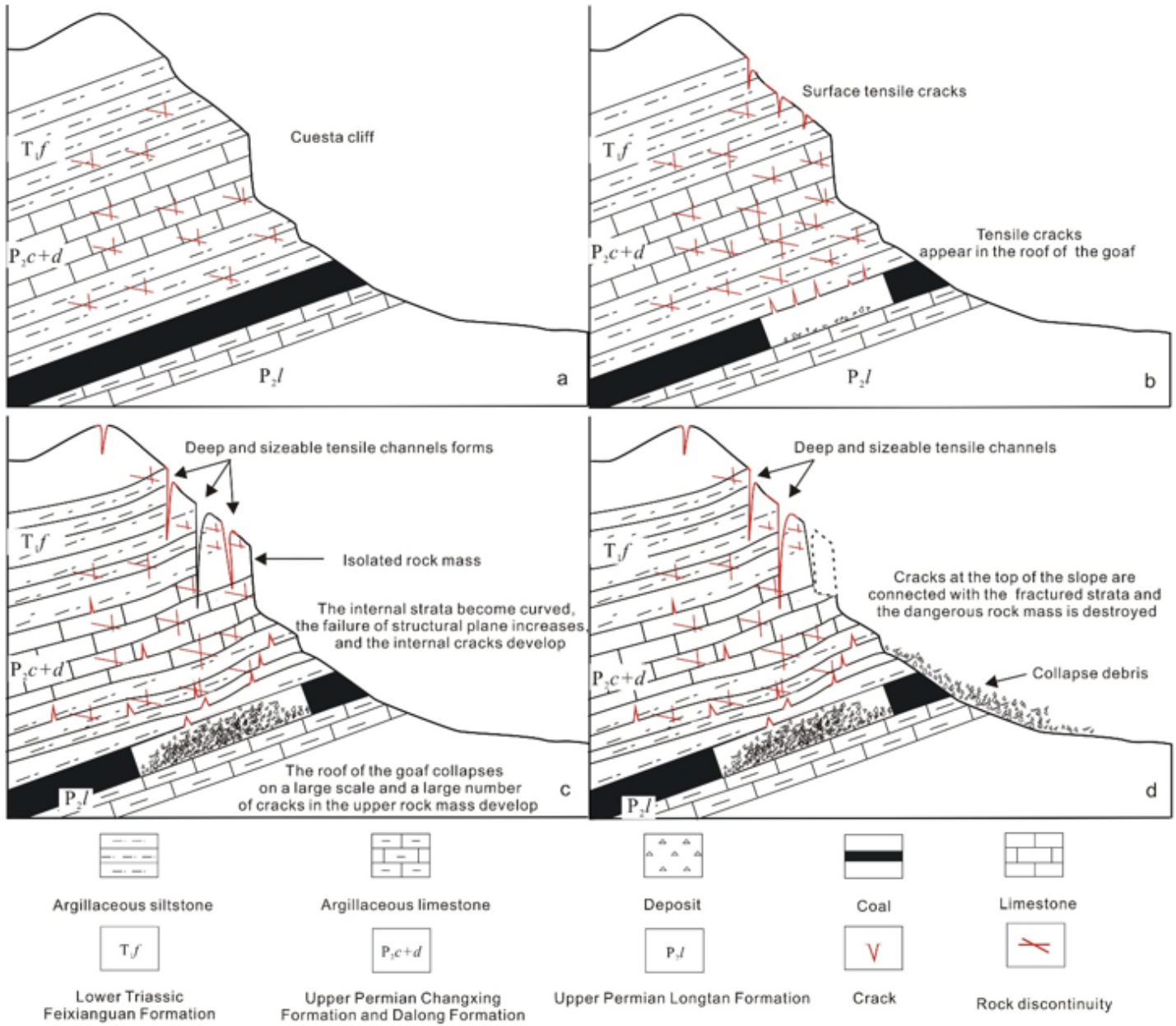
Figure 10

Deformation mode of mining-induced landslides identified by remote sensing and field verification; (a) remote sensing identification of the natural unloading stage; (b) field verification of the natural unloading stage; (c) remote sensing identification of the mining disturbance stage; (d) field verification of the mining disturbance stage; (e) remote sensing identification of the displacement acceleration stage; (f) field

verification of the displacement acceleration stage; (g) remote sensing identification of the slope failure stage; (h) field verification of the slope failure stage

Figure 11

Deformation pattern of a mining-induced landslide; (a) natural unloading stage; (b) mining disturbance stage; (c) displacement acceleration stage; (d) slope failure stage